

Investigating motion blur and temporal aliasing from time-lapse electrical resistivity



Dale Rucker

hydroGEOPHYSICS, Inc, 2302 N Forbes Blvd, Tucson, AZ 85745, United States

ARTICLE INFO

Article history:

Received 4 May 2014

Accepted 17 September 2014

Available online xxxx

Keywords:

Electrical resistivity

Monitoring

Time-lapse

Moment analysis

Image appraisal

ABSTRACT

Geophysical monitoring through time-lapsed resistivity imaging is investigated to determine detrimental effects resulting from temporal smear. Temporal smear can be divided into motion blur and temporal aliasing, with motion blur attributed to an extended sample integration time relative to the velocity of a moving target, thus giving rise to reproduced targets that are distorted versions of the real target shape. Aliasing results from undersampling across time and may give a discontinuous movement. The degree to which each aspect of smear affects target properties described by spatial moment analysis depends on the spatial resolution of the imaging method and the degree to which temporal degradation is applied. For synthetic models with relatively high spatial resolution, aliasing effects were slight except in cases where the minimal number of snapshots was acquired to understand the end state condition of the target. Motion blur, on the other hand, had progressive detrimental effects with each level of additional smearing. For field data acquired during subsurface injection with a lower resolution array, the damaging effects from motion blur and temporal aliasing were equivalent. Both aspects showed progressive degeneration of spatial moments with each level of degradation. To combat this problem in the short term, it is recommended to acquire resistivity data as rapidly as possible and sacrifice some spatial resolution to enhance temporal resolution. In the future, there may be methods adopted from motion photography to deblur target motion by using the point spread function. Aliasing, however, can only be solved through continuous sampling.

© 2014 Elsevier B.V. All rights reserved.

1. Introduction

The electrical resistivity geophysical method is a popular means by which to remotely monitor hydrogeological changes, owing to major advances in instrumentation, survey design, and data inversion techniques (Loke et al., 2013). The temporal variability in resistivity has been directly linked to changes in moisture content (Michot et al., 2003), contaminant concentration (Wilkinson et al., 2010), and temperature-related processes (Hauck, 2002). Quantitatively, the use of time-lapse resistivity to estimate hydraulic parameters has also been extensively applied. For the hydraulic parameter estimation procedure, the subsurface undergoes a significant change by introducing an electrically conductive tracer at a source (Camporese et al., 2011; Monego et al., 2010), which is often followed by an extraction at a nearby sink (e.g., Oldenborger and Routh, 2009; Singha and Gorelick, 2005). Over this period, a set of snapshots are gathered and processed using specialized inverse modeling algorithms to reproduce the subsurface electrical conductivity distribution. In turn, the calculated electrical conductivity is used to estimate the time history of the injected tracer, and

attributes of the reproduced anomaly are compared to attributes from a separate flow and transport model for parameter estimation. Overall, the geophysical data and the hydrogeologically-based models tend to agree with reasonable fidelity. However, several have noted a few problems of the estimation procedure including mass underestimation in the electrical conductivity data by up to 75% and inaccuracies in the location and the degree of spread of the geophysical anomaly (Singha and Gorelick, 2005). Reasons for the underperformance of the resistivity method have been placed on low or nonuniform spatial resolution, regularization, and homogenized petrophysical relations.

With the time-lapse resistivity method, a snapshot of the earth is taken periodically, where each snapshot samples a set of potential measurements taken from combinations within a network of electrodes. Depending on the size of the network, the sampling time over which to complete a single snapshot can be significant. Many have tried to minimize this time to avoid “temporal smear” by either reducing the total number of samples within a snapshot (e.g., Singha and Gorelick, 2005; Ward et al., 2010), reducing the size of the network (Pidlisecky and Knight, 2011; Rucker, 2009), or by developing rapid acquisition systems (Ogilvy et al., 2009; Rucker et al., 2014). While the previous studies tackled the problem from the standpoint of acquisition, several others have tried reducing blur during modeling. Kim et al. (2009) tracked the measurement time of each data sequence and

E-mail addresses: drucker@hgiworld.com, druck8240@gmail.com.

inverted images on a discretized time line. Kuras et al. (2009) used an approach to reduce temporal smear by reorganizing the measurement sequence to ensure measurements with similar spatial sensitivity were as close together in time as possible. Doetsch et al. (2012) accommodated temporal smear through spline interpolation of the potential data to estimate hypothetical values back to a fixed point in time.

One potential reason for the underperformance of the hydrogeophysical modeling that has not been given adequate attention is the effects that arise from temporal smearing. Here, temporal smearing is separated into two related components that include motion blur and temporal aliasing, with motion blur attributed to extended sampling integration time relative to target velocity and aliasing resulting from a large time lag between snapshots. To put it in terms of motion photography, blur results from large exposure times, whereby the shutter is open too long relative to the motion of the target. Temporal aliasing is due to a low frame rate and will produce a target motion that appears discontinuous. Both aspects can affect spatially-derived geometric attributes as estimated from time-lapse inverse modeling. In this work we investigate the issue of temporal smear using both synthetic and field-based resistivity surveys as test cases. The synthetic test cases use either moving or growing conductive targets in a homogeneous background. The field based surveys were conducted during shallow subsurface injections. Spatial moments were then computed to compare results within each test case. The results will show the degree to which each aspect of temporal smearing may give rise to similar observations of inaccurate target reproduction noted in the earlier references.

2. Monitoring strategies

A great deal of our understanding of subsurface processes, and in particular those processes that involve mass and energy transport in porous and fractured media, comes from observing them over a finite time window. The frequency at which observations are conducted, however, tend not to be linked to a temporal scale related to appreciable changes for many state variables describing transport. Rather, the frequency of acquisition is likely conducted ad hoc, with a mindset that oversampling is superior to undersampling and data can simply be filtered or reduced to better understand their implications. Networks of environmental sensors deployed to make our observations are now commonly installed with high frequency acquisition rates to collect moisture, temperature, pressure, etc., with little to no additional expense over low frequency equivalents. The only limitations to deployment appear to be continuous reliable power and data storage. The latter may have been solved with the advent of an intelligent web of sensors, which comprise a network of sensor nodes and communications systems that actively transmit their data to a central server (Delin et al., 2005; Hart and Martinez, 2006).

Monitoring the subsurface with geophysical methods is more temporally constrained compared to a network of independent environmental sensors. Each measurement from a pair of electrodes is interdependent upon measurement at other electrodes. While geophysical methods have proven valuable at yielding information regarding the transient nature of water movement in the subsurface, applying the techniques can be relatively expensive and unwieldy, reducing the rate of acquisition to perhaps one or two snapshots over the course of study relative to hundreds or thousands of snapshots that can be acquired with a sensor. For example, only a few practitioners can dedicate a direct-current (DC) electrical resistivity system to a single long-term project and acquire a sufficient temporal perspective to rival its sensor counterpart (e.g., Calendine et al., 2011; Hilbich et al., 2008; Ogilvy et al., 2009; Sjö Dahl et al., 2008; Versteeg et al., 2004). The expense of dedicated computer hardware, cabling, electrodes, and a processing hub is arguably 10 to 100 times greater than a datalogger with an equal number of sensors to electrodes. Yet, in each case cited above,

the geophysical dataset provided a spatially continuous view that allowed a more complete understanding of subsurface processes than could have been likely provided by a more sparsely distributed set of sensors, regardless of sampling frequency. For the remaining group of geophysicists that cannot dedicate resources for long periods of time, conducting a monitoring study is often opportunistic. Due to time and cost constraints, the studies may be shortened or acquired sporadically.

Extensive investigation into applications of resistivity monitoring for a large degree of problem types have revealed a broad range of monitoring strategies, which have been summarized in Fig. 1. The summary involved defining an order (n) for the approximate number of snapshots within a study equating to 2^n . The timing of acquisition is sometimes synchronous, where snapshots are planned to a specific event such as end state capture. Alternatively, acquisition can be more informal and asynchronous, where data are collected regardless of the condition of the subsurface. Most surveys involve either orders 0 or 1 and it is very rare to find an n^{th} order survey (e.g., Rucker et al., 2014). Acquiring and processing data sufficiently fast have large hardware requirements. However, processing of an n^{th} order survey would likely not involve inverse modeling.

Fig. 2 shows graphically the times at which a resistivity snapshot would likely be acquired for both natural and artificial environmental stimuli. A natural stimulus including precipitation or diurnal heating usually has a periodicity in the environmental variable of interest (e.g., moisture or temperature) and examples are shown for monitoring applications of orders 0, 2, or n . Notice that if a low number of snapshots are acquired relatively to the frequency content of the environmental variable, information will be lost associated with temporal aliasing. For artificial stimulus, such as a subsurface injection, several strategies have been used including simple end state capture, semi-continuous, and continuous acquisition. Together, Figs. 1 and 2 outline a systematic means of applying geophysical monitoring and a full understanding of the final monitoring goal may improve survey design and results while reducing costs. However, as will be demonstrated later, a reduced survey cost through lower coverage may increase the uncertainty in the subsurface properties.

3. Theoretical methodology

The time dependent nature of investigating temporal smearing required the use of time-lapse electrical resistivity tomography (ERT). Several have investigated and compared different means by which to conduct time-lapse ERT (e.g., Hayley et al., 2011; Oldenborger et al., 2007). Noted advantages for a temporally constrained time-lapse inversion include penalizing differences across multiple models allowing a smooth transition of target features through time, while also minimizing artifacts of the background (Hayley et al., 2011). In this work, temporally constrained time-lapse inversion is implemented as described in Loke et al. (2014a), which is available in the commercial inversion code RES3DINVx64.

Borrowing from the descriptions in Rucker et al. (2011) and Loke et al. (2014a), the equation for the constrained optimization method describes the relationship between model parameters and measured data. Here, the model parameters in vector \mathbf{r} are the electrical resistivity values at each discretized cell within the model domain. Given the large range over which electrical resistivity may vary and the nonphysical meaning of most negative electrical resistivity, \mathbf{r} usually represents the logarithm of the model resistivity values. The optimization procedure marches along a piece-wise linear path on the error surface using a model updating procedure to calculate a $\Delta\mathbf{r}_i$ at iteration i using information about \mathbf{r}_{i-1} and the sensitivity matrix, \mathbf{J} , containing the partial derivative of data measurements relative to the model parameters. To dampen the effects of noise being amplified through the modeling procedure, various matrix roughness filters in time (M) and space (W), as well as data and model weighting matrices R_d and R_m ,

Order	Datasets (or snapshots)	Purpose	Event Timing	Resource Load	Comments
0	1	Characterization	Asynchronous	Uncommitted	Provides no historical perspective
1	2	Monitoring	Synchronous	Uncommitted	Understand the end state condition
2	>2	Monitoring	Synchronous	Uncommitted	Capture temporal variability, opportunistic
3	Many	Monitoring	Asynchronous	Committed	Semi-continuous monitoring
n	Many	Monitoring	Asynchronous	Committed	Continuous monitoring

low resource commitment, short duration

dedicated resources, long duration

rate slower than decision making capabilities

rate faster than decision making capabilities

Fig. 1. Geophysical monitoring strategies observed in the literature.

respectively are used such that the final mathematical appearance of the optimization scheme is (Loke et al., 2014a):

$$\begin{aligned}
 & \left[J_i^T R_d J_i + (\lambda_i W^T R_m W + \alpha_i M^T R_t M) \right] \Delta r_i \\
 & = J_i^T R_d g_i - (\lambda_i W^T R_m W + \alpha_i M^T R_t M) r_{i-1}.
 \end{aligned}
 \tag{1}$$

The remaining parameters in Eq. (1) include the data misfit vector, g_i , and the spatial (λ_i) and temporal (α_i) dampening factors. R_t is a weighting matrix used by the L1- or L2-norm method for the temporal constraint (Kim et al., 2009). The objective of the optimization procedure is to reduce the misfit between measured and modeled apparent resistivity values in a least-squares sense.

To accommodate all of the temporal data, r incorporates the calculated resistivity values from each snapshot with a final dimension of nt , where n is the number of model parameters and t is the number of snapshots. Similarly the data misfit vector g will have mt components if each snapshot has m data points (Loke et al., 2014a). The $nt \times mt$ sensitivity matrix becomes large when many snapshots are considered (Hayley et al., 2011), but has been shown to be rather sparse with only nmt non-zero elements with computations only being carried out on these elements (Loke et al., 2014a).

After applying the inverse model algorithm to the time-lapse resistivity data, the model resistivity output is interrogated for spatial statistics using geometric moments of orders 0 through 2. The zero-order spatial moment describes the total mass, the first-order moments in x, y , or z are related to the center of target mass along their respective principle directions, and the second-order moments (again along x, y ,

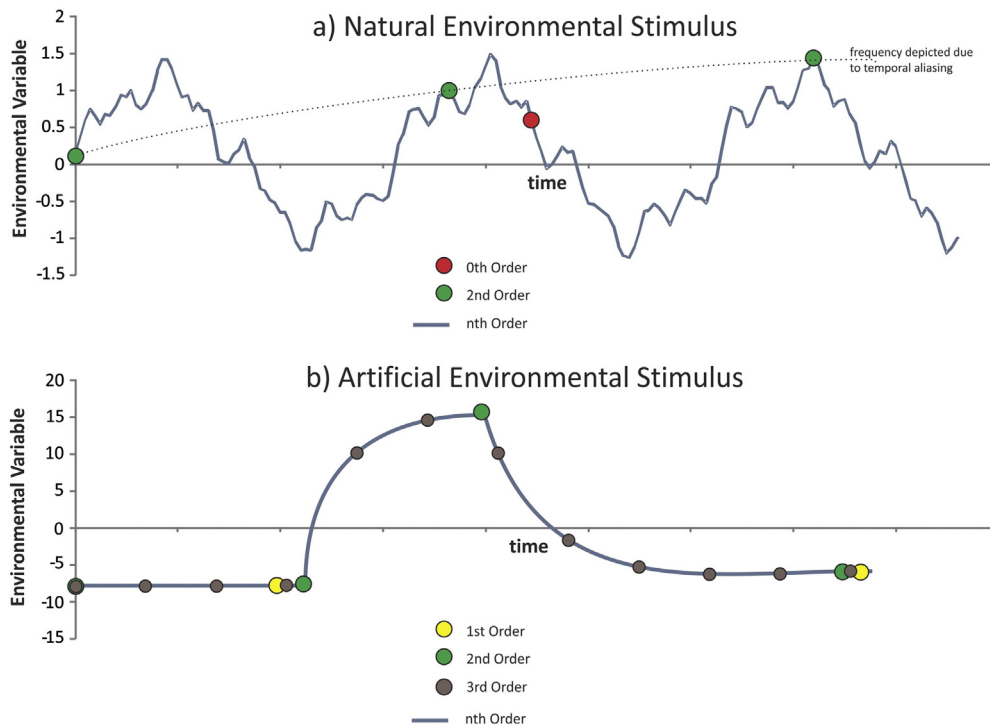


Fig. 2. Graphical representation of monitoring strategies listed in Fig. 1 for a) natural stimulus and b) artificial stimulus.

or z) describe the target spread (Day-Lewis et al., 2007). Many have used these moments to evaluate both geophysical and hydrogeological plumes (e.g., Campoprese et al., 2011; Oldenborger et al., 2007; Singha and Gorelick, 2005).

The moments may be calculated by (Singha and Gorelick, 2005):

$$M_{ijk}(t) = \iiint \Delta C(x, y, z, t) x^i y^j z^k dx dy dz \quad (2)$$

where M_{ijk} is the spatial moment with subscripts defining the particular moment of interest (0, 1, or 2), ΔC is the change in bulk conductivity relative to a background and dx, dy, dz are the cell dimensions of the resistivity model over which the conductivity has been calculated. The zeroth moment is M_{000} . To calculate the center of target mass ($\mu_{100}, \mu_{010}, \mu_{001}$) and target spread ($\sigma_{200}, \sigma_{020}, \sigma_{002}$) along any direction, Eq. (2) is normalized to the zeroth moment:

$$\mu_{100} = \frac{M_{100}}{M_{000}} \quad (3)$$

and

$$\sigma_{100} = \sqrt{\frac{M_{200}}{M_{000}} - \left(\frac{M_{100}}{M_{000}}\right)^2} \quad (4)$$

4. Experimental methodology

4.1. Survey sequence and data acquisition

A data acquisition scheme and a model for temporal smear was developed based on the original model proposed by Chen et al. (1996). Along a time line, t , discrete events are ideally captured instantaneously with a geophysical survey. The results of the ideal unsmear apparent resistivity dataset at time t_0 is represented by $f(x, y; t_0)$. However, our data acquisition system is far from ideal having a noninstantaneous sampling time, Δt , and therefore our real apparent resistivity dataset captured over this finite sampling time is denoted by $g(x, y; \Delta t_{0,1})$. In this framework, data acquisition starts at t_i and is completed at $t_{i+1} = t_i + \Delta t_{i,i+1}$. It is assumed that the next observation begins sometime after according to some monitoring strategy outlined above, so that at time $t_{i+1,i+2} = t_{i+1} + \Delta t_{i+1,i+2}$ the apparent resistivity is represented by $g(x, y; t_{i+1}, \Delta t_{i+1,i+2})$. The timeline of these events is shown in Fig. 3 with baseline conditions occurring before t_1 and the event to monitor (e.g., the injection of a conductive tracer) starts at t_1 . Less robust monitoring systems may take longer than a single Δt to complete, which are further represented in Fig. 3 as $h(x, y; t_2, \Delta t_{1,3})$ and $k(x, y; t_3, \Delta t_{1,4})$. Using synthetic and field examples below, it will be shown that $h(x, y; t_2, \Delta t_{1,3}) \neq g(x, y; \Delta t_{1,2}) + g(x, y; \Delta t_{2,3})$ due to nonlinearities in the modeling likely from the application of temporal regularization. This is an important aspect to many photographic

deblurring algorithms involving the inversion of the point spread function.

4.2. Synthetic modeling

To investigate the adverse effects from temporal smearing, two synthetic test cases were built that aim to isolate various portions of the spatial statistics described by moment analysis. In the first example, a conductive block is moved along a trajectory of constant velocity equaling 0.75 m/snapshot (Fig. 4a). The block is of fixed mass and shape, whereby the zeroth and second spatial moments are constant in time. The first spatial moment changes for each snapshot, first along one direction before being redirected along an orthogonal trajectory. In the second example, a conductive cylindrical block at a fixed location grows with a constant volumetric rate of 6.5 m³/snapshot (Fig. 4b), thereby changing only the zeroth and second spatial moments. Both blocks have resistivity values of 10 Ω -m in a 100 Ω -m background, are 1.2 m tall, and reside from 1.3 to 2.5 m below the surface.

For each synthetic test case, 37 snapshots were evaluated: the first snapshot representing background conditions with a completely homogeneous resistivity and 36 others with changing target conditions. Referring to Fig. 3, the complete set of synthetic data, $S_{complete}$, comprises $\{f(x, y; t_0), f(x, y; t_1), \dots, f(x, y; t_{36})\}$. The data within each snapshot contain a set of apparent resistivity measurements, modeled using RES3DMODx64, along lines of electrodes spaced 3 m in both directions. The Schlumberger array was chosen for our test, creating 18,924 apparent resistivity values for each snapshot in a quasi-3D framework; the hypothetically measured apparent resistivity data were distributed with 12,120 from lines in the x direction and 6804 in the y direction. Additionally, 5% noise was added to the calculated forward dataset. Lastly, the measurement order was randomized and the top 25% of data were retained for all snapshots. Kim et al. (2009) showed that randomization of acquisition will produce better time-lapse images compared to sequential acquisition.

From the group of forward-modeled datasets, temporally constrained, time-lapse resistivity inversion was conducted to replicate the known spatial attributes of the original target. The first trial used all 37 snapshots as a baseline for understanding the best case scenario for target replication and did not consider either aliasing or blurring as a means of degrading target fidelity. The resistivity inversion then tested individually the effects from temporal aliasing and motion blur. For temporal aliasing, seven trials were tested, where each trial progressively skipped over more snapshots to make the frame rate appear lower. The first trial for either an aliased moving target (MA) or aliased growing target (GA) used the background plus every other snapshot during changing target conditions for a total of 19 snapshots as input (e.g., $S_{MA,1} = \{f(x, y; t_0), f(x, y; t_2), f(x, y; t_4), \dots, f(x, y; t_{36})\}$). The modeling for the last trial contained only the background and last snapshot ($S_{MA,7} = \{f(x, y; t_0), f(x, y; t_{36})\}$).

Investigating motion blur was more involved. Given that a synthetic model will provide an instantaneous unsmear image, $f(x, y; t_i)$, steps

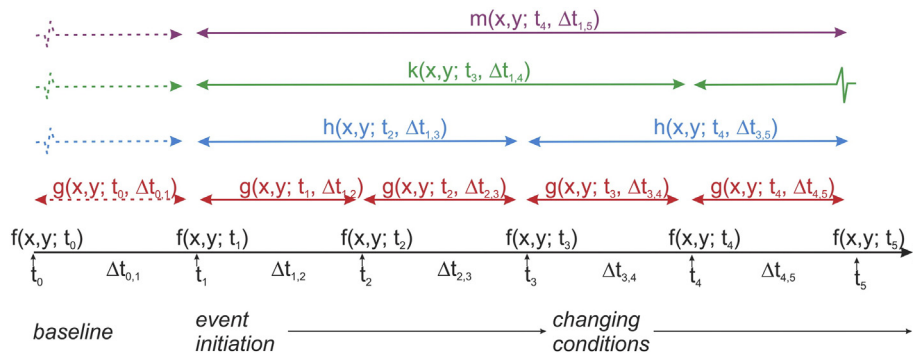


Fig. 3. Graphical description of temporal smear of geophysical data acquired along a continuous time line, t (adapted from Chen et al., 1996).

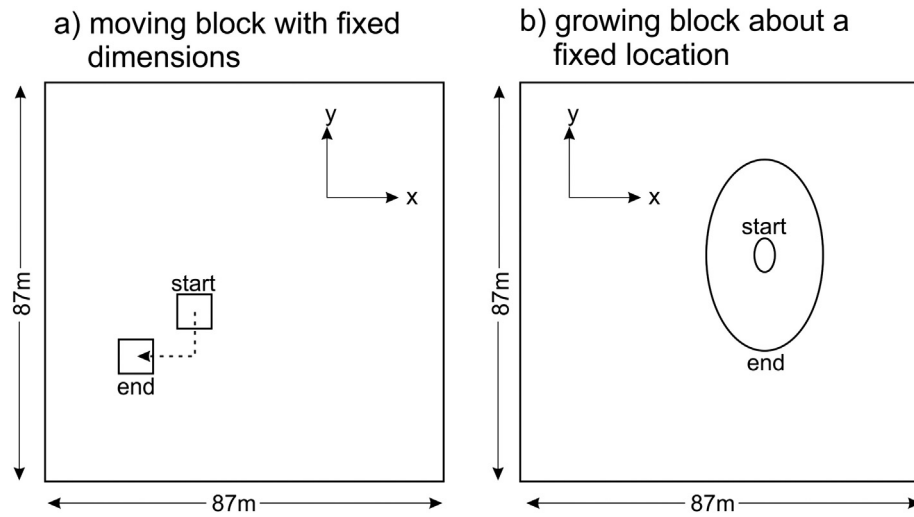


Fig. 4. Geometry of the synthetic models used in the temporal smearing investigation.

were taken to make the acquisition time to be more in line with a real resistivity meter. Seven trials were evaluated by progressively taking subsets of data from sequential snapshots and recombining to make a new snapshot. For example, the first trial for both moving (MB) and growing (GB) blurred targets was reduced to 18 new snapshots by taking the first half of $f(x,y; t_1)$ and the second half of $f(x,y; t_2)$, thereby creating a new snapshot resembling $h(x,y; t_2, \Delta t_{1,3})$. The set of snapshots for trial 1, including the background are represented as $S_{MB,1} = \{f(x,y; t_0), h(x,y; t_2, \Delta t_{1,3}), h(x,y; t_4, \Delta t_{3,5}), \dots, h(x,y; t_{36}, \Delta t_{35,37})\}$. The second trial was created by taking 33% of data each from three original sequential snapshots to create a model with 12 new smeared snapshots resembling $k(x,y; t_{i+2}, \Delta t_{i+3})$. The last trial

comprised of one new snapshot by combining subsets of apparent resistivity data from the 36 original snapshots containing the information with changing target conditions, perhaps resembling the acquisition speed of a single channel resistivity meter. The same procedure was applied to both synthetic data sets and the total number of synthetic trials was 30. Table 1 lists the characteristics for each trial.

Fig. 5 shows the resistivity results for the last snapshot of several trials. The data are presented as a horizontal slice at a depth of 1.75 m through the center of the target. The top two plots show the base case for the moving and growing target, which appear to represent the target shape and location well. The resistivity amplitude for the inverted models is somewhat dampened and the edges smoothly transition to the background. The targets were modeled with a 10 Ω -m value and the lowest values in the inversion model are 48 and 35 Ω -m for the moving and growing target cases, respectively. Additionally, the background resistivity was modeled with a value of 100 Ω -m, but is represented in the final inversions as having values in the range of 94 to 97 Ω -m. Dampened and smooth reproductions of a target and background are well known in resistivity imaging due to the spatial regularization procedure employed. One additional faint feature observed in the moving target model of trial M.1 is a low resistivity tail behind the target. The resistivity values of the tail are on the order of 91–94 Ω -m and could easily be interpreted as noise within the background if information about target trajectory was unknown.

The middle row of models in Fig. 5 presents the moving and growing target cases with nine snapshots, with the last snapshot of the series plotted. When comparing the degree to which the target is dampened, the results of motion blur appear to be more affected than aliasing and both are more dampened compared to the base cases in M.1 and G.1. Additionally, the effects from the tail behind the moving target in MA.3 and MB.3 are only slightly more pronounced compared to M.1. and the bottom edge of the growing target in GB.3 is misshapen.

The last row of models in Fig. 5 shows the extreme effects from aliasing and blur. The temporally aliased models were developed by only considering the background and the last snapshot. The blurred snapshot was created by taking a small portion of data from each of the 36 available snapshots. Interestingly, aliasing of the moving target in MA.7, representing simple end state capture, shows little further degradation than MA.3. The aliased growing target of GA.7 appears to be more dampened and distorted than its counterpart in GA.3. However, the degree to which blurring affects either a moving (model MB.7) or growing (GB.7) target can be characterized as severe. The blurred moving target almost blends completely into the background and the only evidence of its existence is attributed to the slightly lowered resistivity associated with the target's trajectory. The growing blurred target

Table 1

Description of synthetic model trials. Trials M.1 and G.1 were conducted with all available snapshots and were considered the baseline with no smearing or aliasing affecting acquisition and modeling.

Trial	Synthetic model	Number of snapshots (without background)	Type of temporal smearing
M.1	Moving target	36	None
MA.1	Moving target	18	Aliasing
MA.2	Moving target	12	Aliasing
MA.3	Moving target	9	Aliasing
MA.4	Moving target	6	Aliasing
MA.5	Moving target	4	Aliasing
MA.6	Moving target	2	Aliasing
MA.7	Moving target	1	Aliasing
MB.1	Moving target	18	Blurring
MB.2	Moving target	12	Blurring
MB.3	Moving target	9	Blurring
MB.4	Moving target	6	Blurring
MB.5	Moving target	4	Blurring
MB.6	Moving target	2	Blurring
MB.7	Moving target	1	Blurring
G.1	Growing target	36	None
GA.1	Growing target	18	Aliasing
GA.2	Growing target	12	Aliasing
GA.3	Growing target	9	Aliasing
GA.4	Growing target	6	Aliasing
GA.5	Growing target	4	Aliasing
GA.6	Growing target	2	Aliasing
GA.7	Growing target	1	Aliasing
GB.1	Growing target	18	Blurring
GB.2	Growing target	12	Blurring
GB.3	Growing target	9	Blurring
GB.4	Growing target	6	Blurring
GB.5	Growing target	4	Blurring
GB.6	Growing target	2	Blurring
GB.7	Growing target	1	Blurring

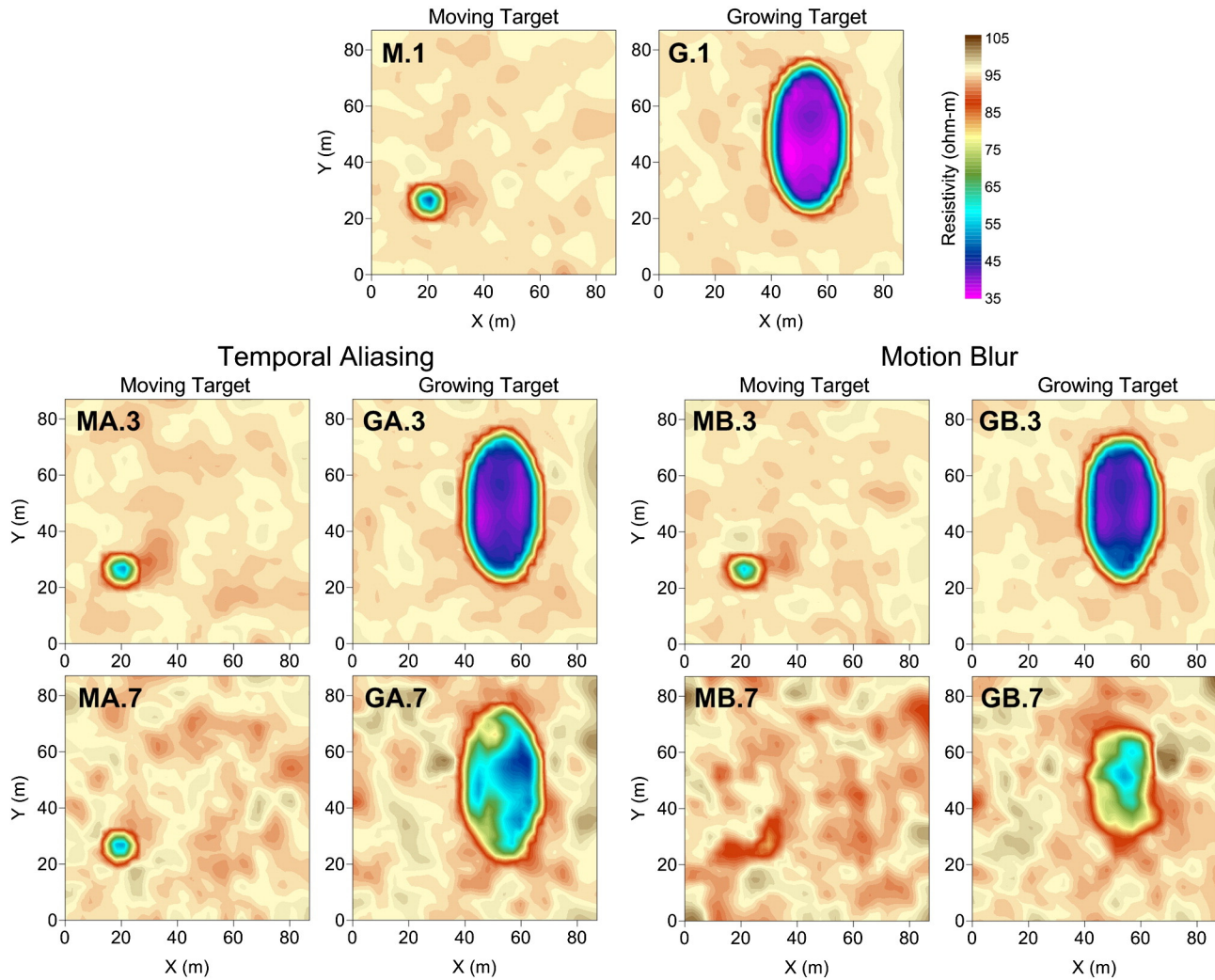


Fig. 5. Resistivity results showing the effects of temporal aliasing and motion blur on synthetic models. Each plot represents a horizontal slice through the three-dimensional model for the last snapshot in each trial. Refer to Table 1 for the description of the trial named in the upper left hand corner of each plot.

is also significantly distorted where the aspect ratio has changed from an original 2:1 to 1.41:1 at approximately 66% of the correct size.

Quantitatively, the attributes of the targets can be observed in Fig. 6, where the spatial moments for each of the models are compared against known conditions and against models representing best case scenarios for resistivity without temporal smearing (M.1 and G.1). For total mass in the top row of plots, all models are underestimating the known conditions. Focusing on temporal aliasing, the best performing model shows a 40% mass underestimation for the moving target test and up to 48% for the growing target at the lowest volume and 9% at maximum volume. The degree by which the underestimation worsens as a function of total number of snapshots is minor but observable. This is in contrast with the results from motion blur of a moving target, where trials with many snapshots perform reasonably well but the last two trials with significant smearing perform poorly. The growing target shows a progressive degradation of mass recoverability with each trial.

For the first spatial moment calculations, or centroids, the aliased models for a moving target tend to capture the target's trajectory with high fidelity along both principle directions. The models for the stationary growing target show minor noise about the known location. Blurred models show progressive degradation of the target centroid with decreasing number of snapshots. For the moving target case, the lingering tail behind the main target is making the target appear to lag. For the growing blurred target, the centroid should be constant and the trials show only a minor amount of scatter around the correct value (less

than 0.5% deviation) with the exception of the last two trials having significant scatter.

The target spread in both x and y directions also shows the same general trends as mass, with the aliased models exhibiting some level of underperformance relative to known conditions but performing on par with the best case scenario. For the blurred moving target, where the second spatial moment should be constant, all but the last two trials with significant blurring perform as well as the aliased models. The blurred trials for the growing target exhibit a progressive degradation with increased blurring, and become extreme in cases of extreme blurring. The contours of resistivity in Fig. 5 for model GB.7 confirms the degree of deformity in target reproduction for the case of extreme blurring.

4.3. Field examples

Two field examples are presented that align with the modeling philosophy and dataset construction as the synthetic test cases. Both field datasets comprise of a number of snapshots acquired during changing subsurface conditions, whereby an injection well was placed within an engineered rock pile (or heap) for the purpose of enhancing the leaching process of low grade metallic ore. In the first example, the injection was in a copper heap, with chrysocolla as the major copper mineral and sulfuric acid as the reagent. In the second example, the experiment took place in a gold heap, with gold mineralization occurring

Moving Target

Growing Target

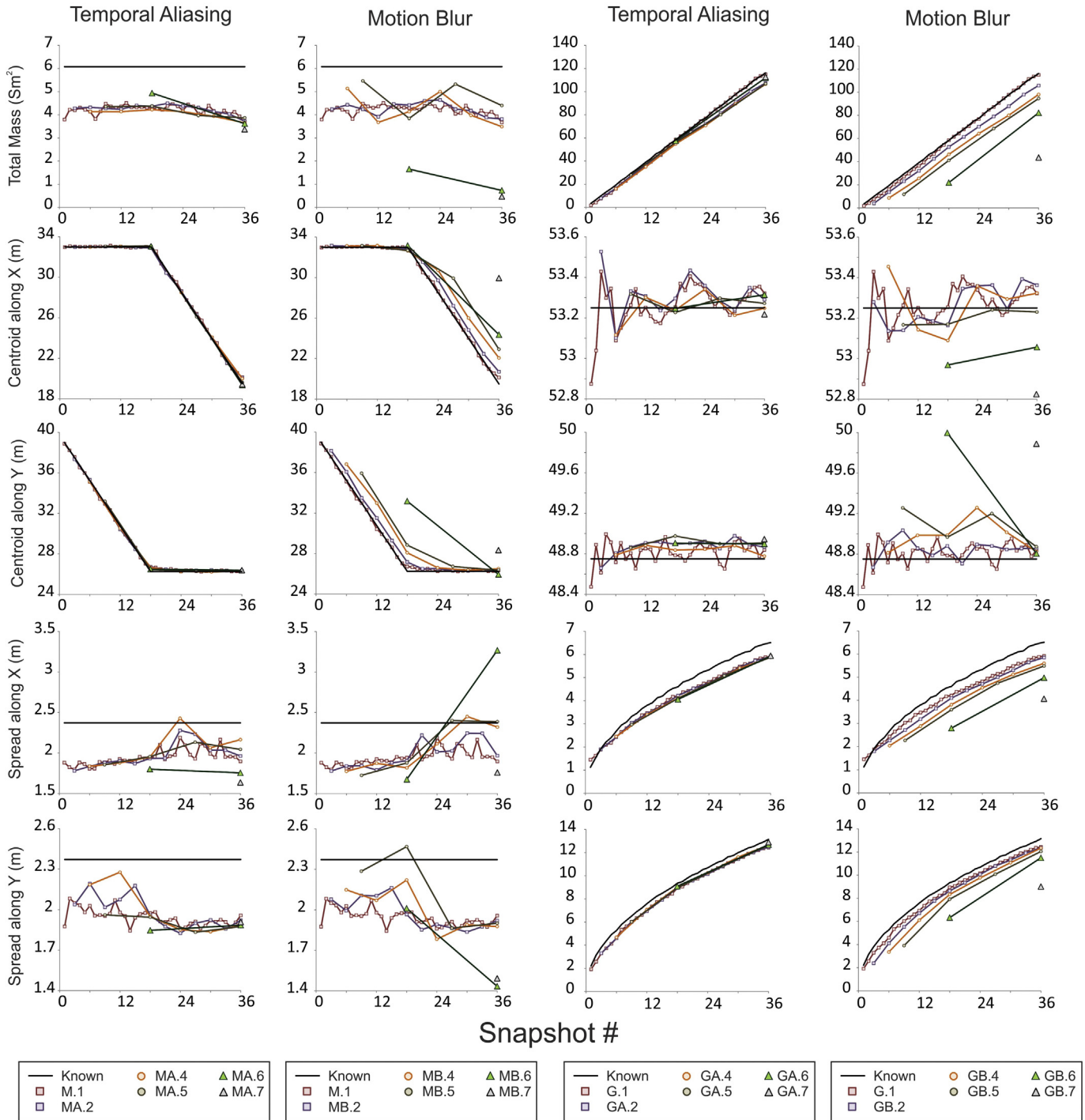


Fig. 6. Spatial moments of the synthetic models with moving and growing targets. Aliased and blurred results are segregated along columns, while the spatial moments are in rows, including the zeroth (total mass), first (centroid), and second (spread) moments.

early in the history of the mine as gold-telluride veins with quartz, pyrite, and fluorite and later from deposits of disseminated native gold attached to pyrite. The reagent for the gold leaching was sodium cyanide.

The differences in the two field examples manifested in the construction of the heaps, grain size distribution of the ore, and injection protocol. For the copper heap, the material was finer-grained with a P_{80} (i.e., probability that 80% of the grains passing a sieve) on the

order of 1 cm and approximately 25% passing a 0.1 mm mesh sieve. At the injection site, the material was placed along flat-lying lifts between 4.5 and 7.5 m to an ultimate height of 50 m. Part way through the heap construction, ore placement changed from truck dumping to retreat stacking due to undesirable compaction effects from heavy mining equipment running over moist fine-grained material. The stacked ore alleviated the compaction issue and increased percolation. At the gold mine, the ore was more uniform and coarser-grained, with a P_{80} of

approximately 2 cm. The injection area was constructed of lifts of approximately 15 to 30 m with an ultimate height of 150 m. The lifts were not flat-lying and instead had significant structure developed from end dumping with trucks. Compaction was not an issue on the gold heap. The expectation of changing target conditions by injecting into these different materials was a simple growing stationary target for the copper experiment having a fixed first spatial moment and a moving growing target for the gold experiment, where the zeroth, first, and second spatial moments changed in time.

The reagent injections occurred across a 3 m screened interval at depths of approximately 30.5 and 33.5 m for the copper and gold experiments, respectively. In both cases, the injections were started in the morning and completed in late afternoon. The copper heap injection remained steady at a flow rate of approximately 1700 L/min for 7.5 h. The gold heap injection flow rates increased from 3200 L/min after 4.5 h to 7800 L/min; the injection period lasted for 9.5 h on the gold heap. Underneath both heaps was a plastic liner to capture the metal-impregnated solution, which eventually directed it to a pond for interim storage before processing to recover the metal in a solvent extraction/electrowinning process.

To capture the highly dynamic reagent plumes, a rapid high-channel resistivity system was deployed to the mines. In both cases, 168 electrodes were used in a pole–pole configuration. The sampling time (Δt) for the system including reciprocals was approximately 23 min, which created over 28,000 data values for each snapshot. The snapshots were captured continuously throughout the injections with 20 snapshots during the copper heap injection and 29 snapshots during the gold heap injection. Additionally, both experiments recorded a background snapshot prior to the start of injections for the day. Fig. 7 shows the layout and scale of both sites. The surface electrodes were placed in radials outward from the injection well, with some infill electrodes in areas of low resolution. For the copper heap, electrodes were also placed within the annulus of nearby injection and sampling wells, which were cased in plastic. For the gold heap, the injection well was cased in steel, which acted as a long electrode. Other borehole electrodes were placed in open holes and backfilled with native material, similar to the description in Rucker et al. (2014). The share of surface and borehole electrodes was nearly equal.

To create a baseline to which to compare the effects from temporal aliasing and motion blur, a time-lapse, temporally constrained inversion was conducted that included all snapshots for the respective experiments. Apparent resistivity data input to the models included only those combinations that met strict reciprocal error cut-off limits equal to 10% for the copper heap and 5% for the gold heap; the average

reciprocal apparent resistivity was used as the final input value. The higher limit for the copper heap was deemed necessary because the data were noisier due to the extreme conductive nature of the reagent and the significant self-potentials generated from the dissolution of oxide and oxidation–reduction reactions of sulfide minerals. Other input to the models included upper and lower zero flux boundaries developed from surface and liner topographies. The results of the baseline models are presented in Fig. 8a and c, and show the resistivity for the background with a cutaway to expose internal values near the injection well. The background plots confirm that the copper heap is much more conductive than the gold heap owing to the higher ionic strength of the copper sulfate versus sodium aurocyanide. The percent change in conductivity from background for two snapshots are presented in the bottom row of Fig. 8. The plots of changes in conductivity show two rendered bodies representing an increase of 1% from background conductivity, with an inner darker plume midway through the day's injection and the outer transparent plume at the end of the injection. The higher flow rate and pressure for the gold heap allow a larger dispersal of solution, reaching out to 43 m from the injection well. The coverage for the copper injection is approximately 14 m outward from the injection well. In both cases the solution is dropping to the liner and flowing outwards to the pond, directed by the topography of the liner.

Aliased and blurred models were created from the full set of snapshots, using similar input file construction as described for the synthetic models. The difference, however, was that for the field experiment, $f(x,y;t)$ does not exist and all newly created time-lapse datasets started with $g(x,y; t_{i+1}, \Delta t_{i+1,i+2})$. For the copper experiment, the 20 snapshots during active injection were degraded using five trials each for blurred and aliased models and each was compared to the results of the base case with no degradation. Seven new trials were constructed to test blurring and aliasing with the data from the gold experiment and Table 2 lists the series of models run for both injections.

Figs. 9 and 10 show the spatial moment summaries for both injections, focusing mainly on the changes occurring along the x axis. Additionally, both figures present the base case scenario of all snapshots as well as flow rate or cumulative injection volume data from the injection well. For the copper injection, the results for both aliased and blurred models look strikingly similar. The zeroth moment representing an estimate of total mass shows that for each level of degradation the estimate of total mass declines significantly with the trial representing simple end state capture (CA.5 and CB.5) having the lowest estimated mass. For the centroid along the x axis in the middle row of Fig. 9, the change through time is slight for the base case and moves only a couple of meters away from the injection point. All models follow a trajectory of

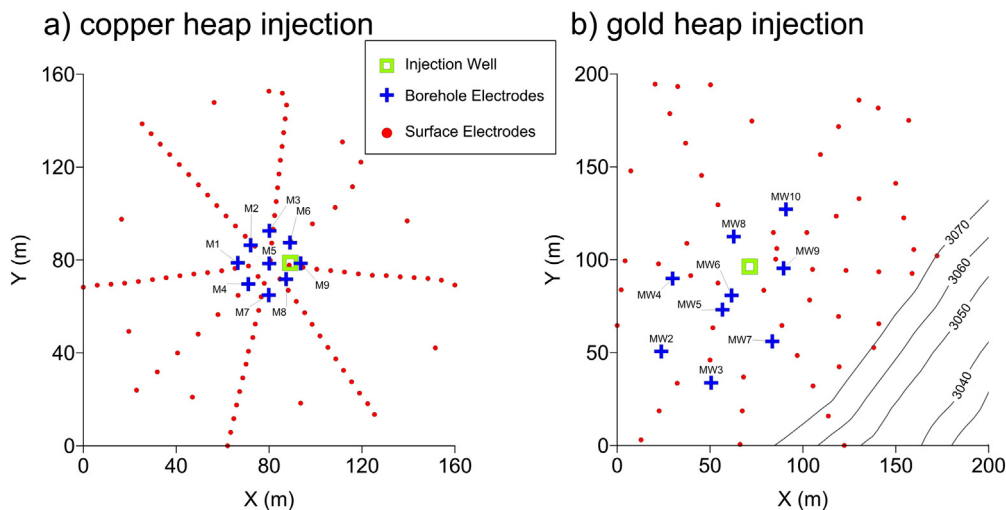


Fig. 7. Layout of injection wells and resistivity survey on a) copper heap and b) gold heap. The elevation of the surface for the copper heap is 1207 m and the elevation contours for the gold heap are in meters.

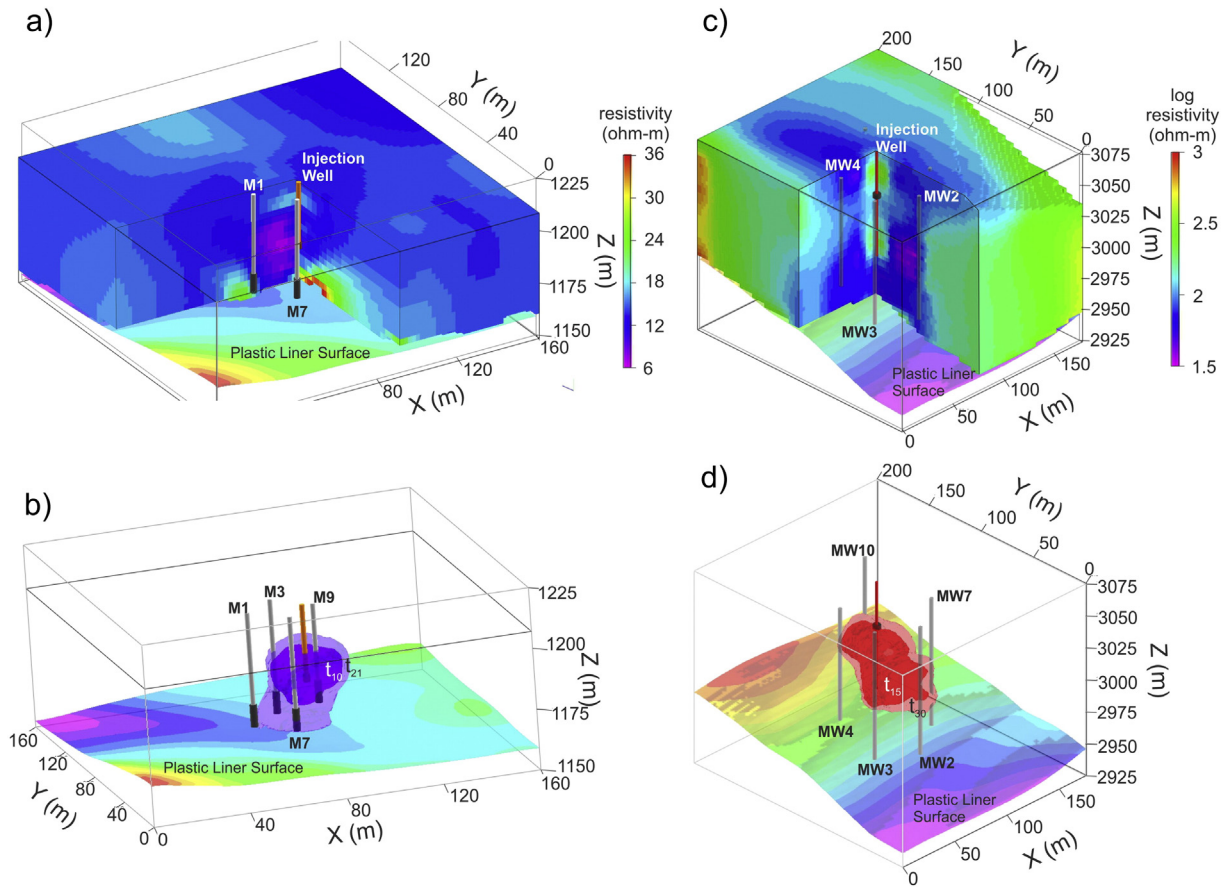


Fig. 8. Time-lapse resistivity inversion results for the copper and gold heap injection experiments, showing a) background resistivity (t_0) for the copper heap with cutaway to expose the conditions near the injection well, b) solid bodies of 1% change in conductivity relative to background for t_{10} and t_{21} , c) background resistivity (t_0) in log scale for the gold heap with cutaway to expose the conditions near the injection well, and d) solid bodies of 1% change in conductivity relative to background for t_{15} and t_{30} . The insulating plastic liner is also shown with color contours representing topography.

moving west and a few replicate the slight eastward tack after the first hour or two of the injection start time. The plume spread, calculated by the second spatial moment, shows similar results to the total mass, namely a progressive decline in spread with each level of degradation.

Fig. 10 also shows that the differences between aliased and blurred models are very similar for the gold injection experiment. Additionally, as the temporal resolution becomes more degraded with fewer snapshots, the further removed the end points are from the base case. For total mass, the final end state capture models with one snapshot (AA.7 and AB.7) shows less than 2% mass recovery relative to the base case. For the trajectory of the reagent plume (center row in Fig. 10), there does appear to be slightly better performance by the aliased models compared to the blurred models. The increase in flow rate at about 11:30 am causes a marked shift in directionality, which appears to manifest in the base case approximately 1 h before the start of the actual flow increase. The plume spread along the x axis also shows a jump start in increased size before the flow is ramped up. This may suggest that even the rapid acquisition system with sampling time of about 23 min may be a little too slow for this particular problem.

5. Discussion

It is clear that temporal smear of resistivity surveys, resulting from either aliasing or blurring, affects the outcome of time-lapse inversion using temporal constraints. The temporal constraints are incorporated to smooth variation in model parameters across time, much like the spatial constraints are used to smooth model parameters across space.

Table 2

List of copper (C.x, CA.x and CB.x) and gold (A.x, AA.x, and AB.x) time-lapse models for the injection experiments.

Trial	Metal mine	Number of snapshots (without background)	Type of temporal smearing	Percent of total mass relative to base case
C.1	Copper	20	None	-
CA.1	Copper	10	Aliasing	44.6
CA.2	Copper	7	Aliasing	31.7
CA.3	Copper	4	Aliasing	14.7
CA.4	Copper	2	Aliasing	7.8
CA.5	Copper	1	Aliasing	4.1
CB.1	Copper	10	Blurring	48.5
CB.2	Copper	7	Blurring	32.3
CB.3	Copper	4	Blurring	19.1
CB.4	Copper	2	Blurring	10.7
CB.5	Copper	1	Blurring	3.7
A.1	Gold	29	None	-
AA.1	Gold	15	Aliasing	43.2
AA.2	Gold	10	Aliasing	15.5
AA.3	Gold	6	Aliasing	8.1
AA.4	Gold	4	Aliasing	4.7
AA.5	Gold	3	Aliasing	3.3
AA.6	Gold	2	Aliasing	1.9
AA.7	Gold	1	Aliasing	1.2
AB.1	Gold	29	Blurring	32.2
AB.2	Gold	15	Blurring	17.5
AB.3	Gold	10	Blurring	10.1
AB.4	Gold	6	Blurring	6.3
AB.5	Gold	4	Blurring	4.4
AB.6	Gold	3	Blurring	3.0
AB.7	Gold	2	Blurring	1.1

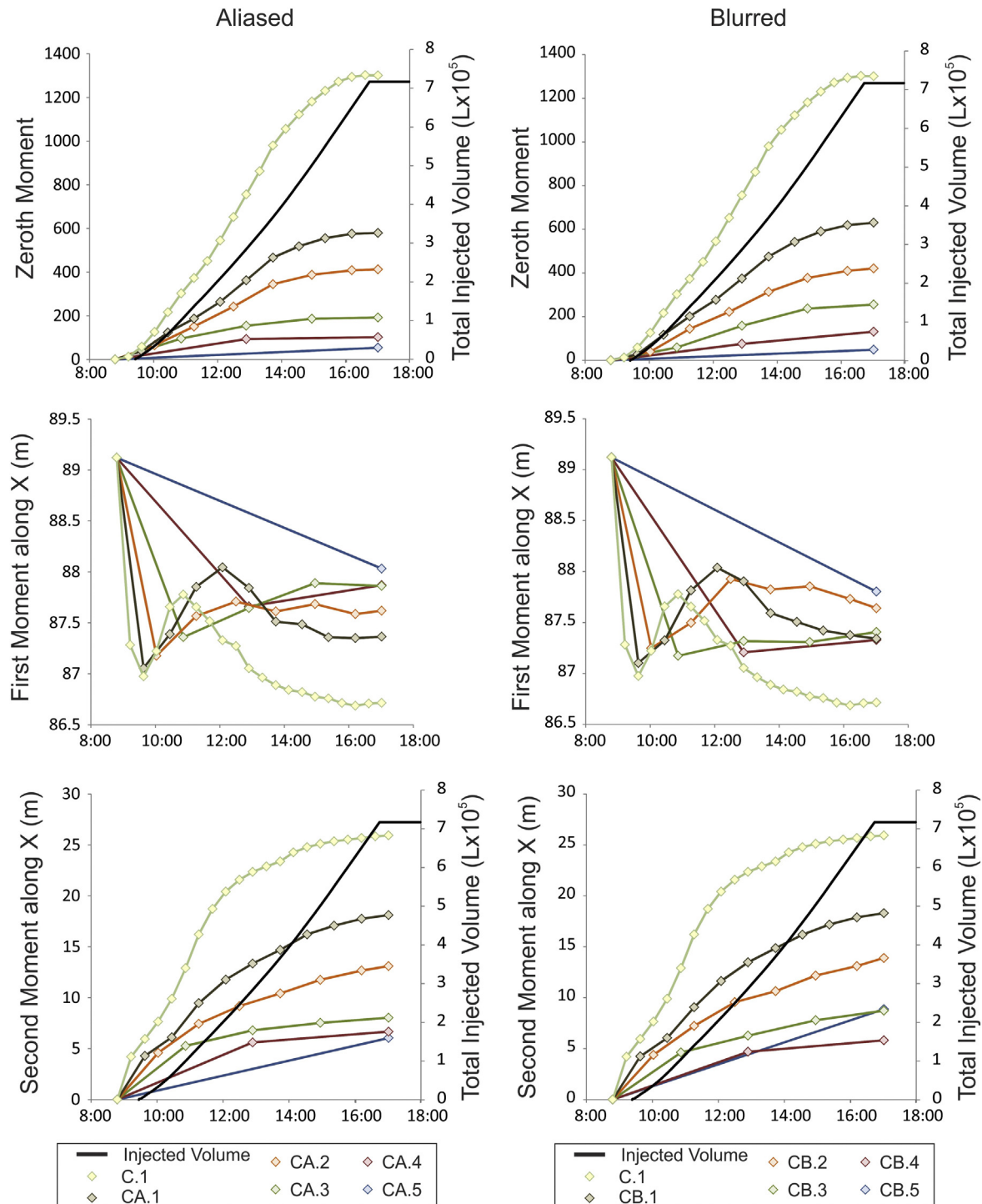


Fig. 9. Spatial moments for the copper mine injection experiment. Time-lapse resistivity models were completed for a base case with all available snapshots, aliased snapshots, and blurred snapshots. The figure focuses on the zeroth moment to obtain an estimate of mass, and the first and second moments along the x axis only to demonstrate the level of degradation from each trial with fewer snapshots. The description of a specific trial is given in Table 2.

With each level of degradation resulting from fewer snapshots, the results are progressively worse relative to a base case with no degradation. The synthetic models show that aliasing has only minimal impact, and the spatial moments of the target in the inversion model match the base case fairly well except in the most severe aliasing case involving simple end state capture. However, the field data show the same level of degradation between aliasing and blurring. Arguably, the models resulting from field data are at much a lower spatial resolution due to the type of array, size of the domain, and depth of the target relative to the synthetic models. Rucker (2014) explored the issue of spatial

resolution by increasing the depth of the moving target example and confirms that lower spatial resolution can increase the damaging effects from aliasing.

Motion photography research reveals a variety of means to tackle the problem of smear from both aspects of acquisition and post processing. For acquisition, cameras with high-speed shutters have been developed, where each snapshot in a sequence is acquired by keeping the shutter open for an infinitesimally short duration. This is akin to the methodology presented here, by using a rapid acquisition system to reduce the sampling time. The downside of high speed acquisition

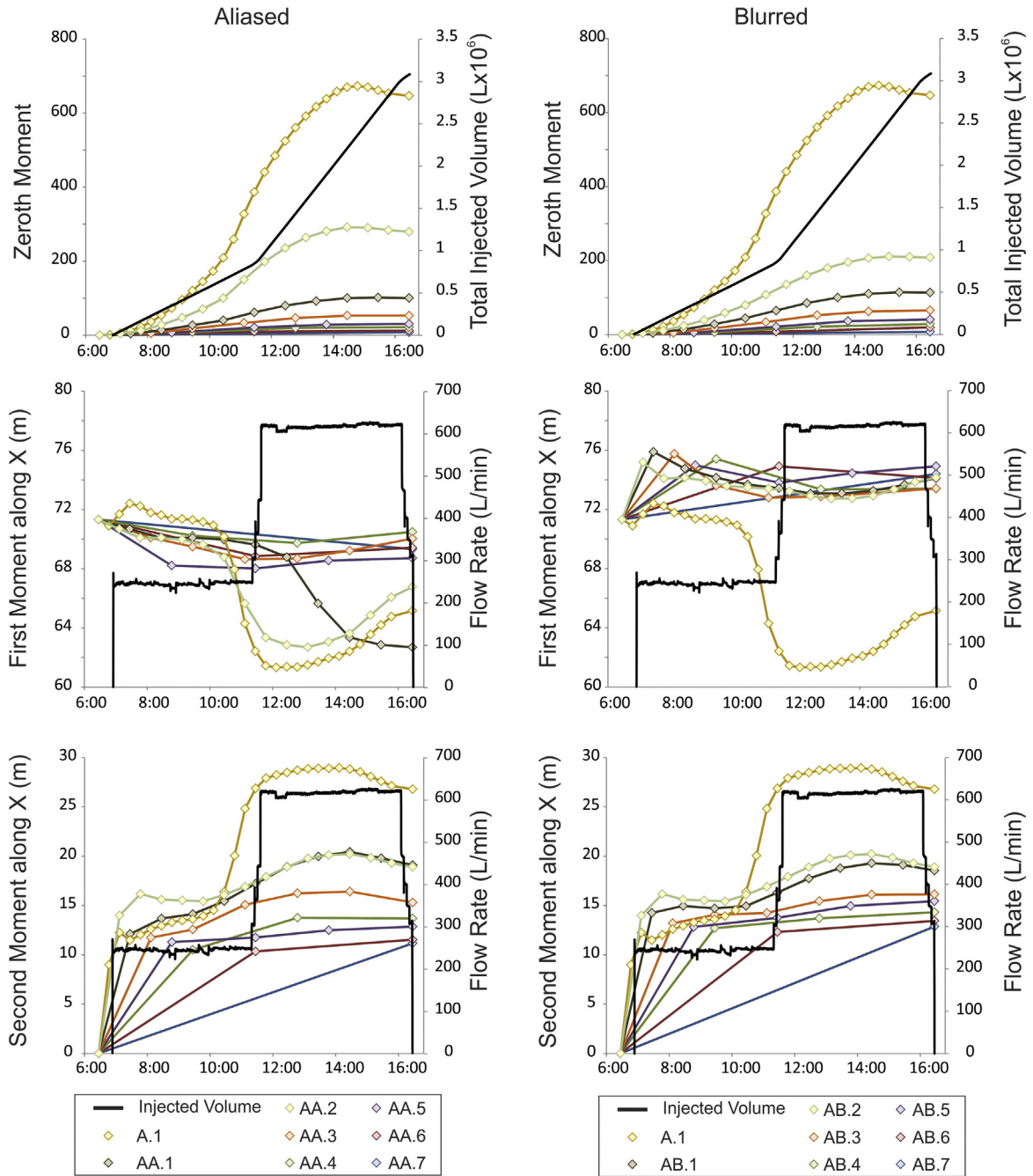


Fig. 10. Spatial moments for the gold mine injection experiment for the base case, aliased models, and blurred models. The figure focuses on the zeroth moment and the first and second moments along the x axis. The description of a specific trial is given in Table 2.

systems is that the amount of information collected during the snapshot is low in order to reduce blur. A complete set of three-dimensional data with the pole–pole array can be acquired much more quickly than either a pole–dipole or dipole–dipole arrays based on the large number of pairs offered by the latter. Unfortunately, the information content as measured by model resolution is low for the pole–pole. A significantly reduced set of dipole pairs can be collected instead, and different arrangements were tested in Oldenborger et al. (2007). Sports photography uses a moving camera on a track to keep the main target in focus. Similarly, Stummer et al. (2004) and Furman et al. (2007) describe an acquisition methodology that locally focuses on a target by choosing electrode pairs that maximizes sensitivity of those pairs. Tests for sequential experimental design were subsequently tested in Wilkinson et al. (2013). If the resistivity monitoring program were directly coupled

with a flow and transport code, a predicted target location could be obtained and a new local set of electrode pairs be used to keep the target in focus. The sampling time could be reduced significantly by choosing the best subset of measurements. However, computation time may be prohibitive to implement unless these locally optimal pairs are identified in a matter of a few minutes.

In post processing, the key element to deblurring photographic images has been inverting the point spread function (PSF). The PSF describes the response (or filter) of an imaging system to a target and is ideally an impulse function, which is convolved with the original scene to form the photograph. In practice, the PSF is usually a low pass filter due to finite exposure time and will contain nulls in the frequency spectrum (Agrawal et al., 2009). These frequencies are lost, thus making the inversion of the PSF for deblurring ill-posed. Several have developed

specialized techniques to create a PSF that can be inverted, including a fluttered shutter (Raskar et al., 2006), motion invariant photography (Levin et al., 2008), and null filling of the frequency spectrum by combining multiple PSFs (Agrawal et al., 2009).

For the electrical resistivity problem, the PSF is the set of column vectors comprising the resolution matrix (Oldenborger and Routh, 2009). The resolution matrix (\mathbf{T}) may be viewed as a filter applied to the true subsurface resistivities (Stummer et al., 2004), such that:

$$\mathbf{r}^{est} = \mathbf{T} \mathbf{r}^{true} \quad (5)$$

where \mathbf{r}^{est} is the vector of the estimated resistivity and \mathbf{r}^{true} is the true subsurface resistivity. The linearized resolution matrix provides a measure of resolving power for models that are linearly close to the actual model (Oldenborger and Routh, 2009). Ideally, \mathbf{T} is the identity matrix but in practice is asymmetric with values less than one on the diagonal. The PSF then becomes not an impulse, but a blurring filter that may have side lobes and localization errors resulting from an imperfect model replication of the target. If the width of the PSF is significantly broader than the width of the model cell, the model is poorly resolved at that location (Miller and Routh, 2007), and Alumbaugh and Newman (2000) demonstrate a PSF at several locations in an electromagnetic inversion model to show the degree of blurring. When considering the degree to which motion blur also smears image quality, it would appear that simply inverting the PSF to remove the motion aspect would be intractable. For this reason, it may be better to tackle the problem from the standpoint of acquisition.

6. Conclusions

Temporal smear during time-lapse imaging of electrical resistivity targets has been recognized by several geophysicists as a potential problem, at least during the acquisition of such data. The remedy has been to reduce the number of samples in a given time period such that a lower spatial resolution gives rise to a greater temporal resolution. It has been demonstrated here, using both synthetic and field data examples with different degrees of degradation through motion blur and aliasing, that approach is justified. High temporal resolution was shown to be important for mass recovery, trajectory, and target width and low temporal resolution may be contributing to underperformance of joint inversion models aimed at estimating hydraulic properties used to describe mass movement.

The review of work by others and the different monitoring strategies applied to understand the subsurface, at least for an artificial environmental stimulus, reveal that simple end state capture is not a suitable means of monitoring when using temporally constrained time-lapse inversion (e.g., Rucker et al., 2011). Other time-lapse inversion methods were not tested and it may be that the choice of algorithm to investigate this issue is affecting the outcome. Regardless, future monitoring projects with the resistivity method should at least consider the velocity of the target, the number of snapshots, and the speed at which those snapshots can be acquired. Practitioners should also be cognizant of the factors that affect smear and conduct their own tests to understand the degree to which their strategy may be degrading the outcome.

In the short term, overcoming temporal smear is likely solved during acquisition with rapid, high channel resistivity systems. The largest known field-deployable system is 180 channels (Rucker et al., 2014). However, even with a large number of channels, the speed of acquisition for any system will depend on the number of transmitting electrode pairs. This is a good reason for choosing the pole–pole method, as the number of comprehensive combinations is significantly lower than that of either pole–dipole or dipole–dipole. Even though it is known for being a very low resolving array, steps can be taken to increase the resolving power of the data by converting them to a different array (e.g., Rucker, 2012). For a longer view, methods for deblurring from motion photography could be employed to reduce the effects

from smear by taking advantage of an invertible PSF, but only if it is itself a suitable filter for resolving each frame of the moving target. Loke et al. (2014b) demonstrates several PSFs for standard and optimized arrays, with the optimized array exhibiting sharper peaks and narrow widths. There also may be ways to limit the effects from aliasing, as demonstrated by Doetsch et al. (2012), where temporal information lost by undersampling can be interpolated at a higher resolution.

References

- Agrawal, A., Xu, Y., Raskar, A.R., 2009. Invertible motion blur in video. *ACM Trans. Graph.* 28, 1–8.
- Alumbaugh, D.L., Newman, G.A., 2000. Image appraisal for 2-D and 3-D electromagnetic inversion. *Geophysics* 65, 1455–1467.
- Calendine, S., Rucker, D.F., Fink, J.B., Levitt, M.T., Schofield, J., 2011. Automated leak detection of buried tanks using geophysical methods at the Hanford nuclear site. *SAGEEP 2011, Annual meeting of the Environmental and Engineering Geophysical Society*, Charleston, SC, April 10–14, 2011.
- Campoprese, M., Cassiani, G., Deiana, R., Salandin, P., 2011. Assessment of local hydraulic properties from electrical resistivity tomography monitoring of a three-dimensional synthetic tracer test experiment. *Water Resour. Res.* 47, W12508.
- Chen, W.-G., Nandhakumar, N., Martin, W.N., 1996. Image motion estimation from motion smear—a new conceptual model. *IEEE Trans. Pattern Anal. Mach. Intell.* 18, 412–425.
- Day-Lewis, F.D., Chen, Y., Singha, K., 2007. Moment inference from tomograms. *Water Resour. Res.* 34, L22404.
- Delin, K.A., Jackson, S.P., Johnson, D.W., Burleigh, S.C., Woodrow, R.R., McAuley, J.M., Dohm, J.M., Ip, F., Ferré, T.P.A., Rucker, D.F., Baker, V.R., 2005. Environmental studies with the sensor web: principles and practice. *Sensors* 5, 103–117.
- Doetsch, J., Linde, N., Vogt, T., Binley, A., Green, A.G., 2012. Imaging and quantifying salt-tracer transport in a riparian groundwater system by means of 3D ERT monitoring. *Geophysics* 77, B207–B218.
- Furman, A., Ferré, T.P.A., Heath, G.L., 2007. Spatial focusing of electrical resistivity surveys considering geologic and hydrologic layering. *Geophysics* 72, F65–F73.
- Hart, J.K., Martinez, K., 2006. Environmental sensor networks: a revolution in the earth system science? *Earth Sci. Rev.* 78, 177–191.
- Hauk, C., 2002. Frozen ground monitoring using DC resistivity tomography. *Geophys. Res. Lett.* 29, 2016.
- Hayley, K., Pidlisecky, A., Bentley, L.R., 2011. Simultaneous timelapse electrical resistivity inversion. *J. Appl. Geophys.* 75, 401–411.
- Hilbich, C., Hauck, C., Hoelzle, M., Scherler, M., Schudel, L., Volksch, I., Vonder, D., Muhl, M., Mausbacher, R., 2008. Monitoring mountain permafrost evolution using electrical resistivity tomography: a 7-year study of seasonal, annual, and long-term variations at Schilthorn, Swiss Alps. *J. Geophys. Res.* 113, F01S90.
- Kim, J.H., Yi, M.J., Park, S.G., Kim, J.G., 2009. 4-D inversion of DC resistivity monitoring data acquired over a dynamically changing earth model. *J. Appl. Geophys.* 68, 522–532.
- Kuras, O., Pritchard, J.D., Meldrum, P.I., Chambers, J.E., Wilkinson, P.B., Ogilvy, R.D., Wealthall, G.P., 2009. Monitoring hydraulic processes with automated time-lapse electrical resistivity tomography (ALERT). *C. R. Geosci.* 341, 868–885.
- Levin, A., Sand, P., Cho, T.S., Durand, F., Freeman, W.T., 2008. Motion-invariant photography. *ACM Trans. Graph.* 27, 71.
- Loke, M.H., Chambers, J.E., Rucker, D.F., Kuras, O., Wilkinson, P.B., 2013. Recent developments in the direct-current geoelectrical imaging method. *J. Appl. Geophys.* 95, 135–156.
- Loke, M.H., Dahlin, T., Rucker, D.F., 2014a. Smoothness-constrained time-lapse inversion of data from 3-D resistivity surveys. *Near Surf. Geophys.* 12, 5–24.
- Loke, M.H., Wilkinson, P.B., Chambers, J.E., Strutt, M., 2014b. Optimized arrays for 2D cross-borehole electrical tomography surveys. *Geophys. Prospect.* 62, 172–189.
- Michot, D., Benderitter, T., Dorigny, A., Nicoulaud, B., King, D., Tabbagh, A., 2003. Spatial and temporal monitoring of soil water content with an irrigated corn crop cover using surface electrical resistivity tomography. *Water Resour. Res.* 39, 1138.
- Miller, C.R., Routh, P.S., 2007. Resolution analysis of geophysical images: comparison between point spread function and region of data influence measures. *Geophys. Prospect.* 55, 835–852.
- Monego, M., Cassiani, G., Deiana, R., Putti, M., Passadore, G., Altissimo, L., 2010. A tracer test in a shallow heterogeneous aquifer monitored via time-lapse surface electrical resistivity tomography. *Geophysics* 75, WA61–WA73.
- Ogilvy, R.D., Kuras, O., Meldrum, P.I., Wilkinson, P.B., Gisbert, J., Jorroto, S., Frances, I., Pulido Bosch, A., 2009. Automated time-lapse electrical resistivity tomography (ALERT) for monitoring coastal aquifers. *Near Surface Geophysics* 7, 367–375.
- Oldenborger, G.A., Routh, P.S., 2009. The point-spread function measure of resolution for the 3-D electrical resistivity experiment. *Geophys. J. Int.* 176, 405–414.
- Oldenborger, G.A., Knoll, M.D., Routh, P.S., LaBrecque, D.J., 2007. Time-lapse ERT monitoring of an injection/withdrawal experiment in a shallow unconfined aquifer. *Geophysics* 72, F177–F187.
- Pidlisecky, A., Knight, R., 2011. The use of wavelet analysis to derive infiltration rates from time-lapse one-dimensional resistivity records. *Vadose Zone J.* 10, 697–705.
- Raskar, R., Agrawal, A., Tumblin, J., 2006. Coded exposure photography: motion deblurring using fluttered shutter. *ACM Trans. Graph.* 25, 795–804.
- Rucker, D.F., 2009. A coupled electrical resistivity-infiltration model for wetting front evaluation. *Vadose Zone J.* 8, 383–388.
- Rucker, D.F., 2012. Enhanced resolution for long electrode ERT. *Geophys. J. Int.* 191, 101–111.

- Rucker, D.F., 2014. The effects of temporal smear on resistivity data: a synthetic model test. Society of Exploration Geophysicists Annual Meeting. Society of Exploration Geophysicists, Denver, CO.
- Rucker, D.F., Fink, J.B., Loke, M.H., 2011. Environmental monitoring of leaks using time lapsed long electrode electrical resistivity. *J. Appl. Geophys.* 74, 242–254.
- Rucker, D.F., Crook, N., Winterton, J., McNeill, M., Baldyga, C.A., Noonan, G., Fink, J.B., 2014. Real-time electrical monitoring of reagent delivery during a subsurface amendment experiment. *Near Surface Geophysics* 12, 151–163.
- Singha, K., Gorelick, S., 2005. Saline tracer visualized with three-dimensional electrical resistivity tomography: field-scale spatial moment analysis. *Water Resour. Res.* 41, W05023.
- Sjödahl, P., Dahlin, T., Johansson, S., Loke, M.H., 2008. Resistivity monitoring for leakage and internal erosion detection at Hällby embankment dam. *J. Appl. Geophys.* 65, 155–164.
- Stummer, P., Maurer, H., Green, A., 2004. Experimental design: electrical resistivity data sets that provide optimum subsurface information. *Geophysics* 69, 120–129.
- Versteeg, R., Ankeny, M., Harbour, J., Heath, G., Kostelnik, K., Mattson, E., Moor, K., Richardson, A., Wangerud, K., 2004. A structured approach to the use of near-surface geophysics in long-term monitoring. *Lead. Edge* 23 (7), 700–703.
- Ward, A.S., Gooseff, M.N., Singha, Kamini, 2010. Imaging hyporheic zone solute transport using electrical resistivity. *Hydrol. Process.* 24, 948–953.
- Wilkinson, P.B., Meldrum, P.I., Kuras, O., Chambers, J.E., Holyoake, S.J., Ogilvy, R.D., 2010. High-resolution electrical resistivity tomography monitoring of a tracer test in a confined aquifer. *J. Appl. Geophys.* 70, 268–276.
- Wilkinson, P.B., Uhlemann, S.S., Chambers, J.E., Meldrum, P.I., Oxby, L.S., Kuras, O., 2013. Optimised sequential experimental design for geoelectrical resistivity monitoring surveys. *Near Surface Geoscience*. European Association of Geoscientists and Engineers (EAGE), Bochum, Germany.